



Fourier ptychographic dark field x-ray microscopy

Carlsen, Mads; Ræder, Trygve M.; Yildirim, Can; Rodriguez-Lamas, Raquel; Detlefs, Carsten; Simons, Hugh

Published in:
Optics Express

Link to article, DOI:
[10.1364/OE.447657](https://doi.org/10.1364/OE.447657)

Publication date:
2022

Document Version
Publisher's PDF, also known as Version of record

[Link back to DTU Orbit](#)

Citation (APA):
Carlsen, M., Ræder, T. M., Yildirim, C., Rodriguez-Lamas, R., Detlefs, C., & Simons, H. (2022). Fourier ptychographic dark field x-ray microscopy. *Optics Express*, 30(2), 2949-2962. <https://doi.org/10.1364/OE.447657>

General rights

Copyright and moral rights for the publications made accessible in the public portal are retained by the authors and/or other copyright owners and it is a condition of accessing publications that users recognise and abide by the legal requirements associated with these rights.

- Users may download and print one copy of any publication from the public portal for the purpose of private study or research.
- You may not further distribute the material or use it for any profit-making activity or commercial gain
- You may freely distribute the URL identifying the publication in the public portal

If you believe that this document breaches copyright please contact us providing details, and we will remove access to the work immediately and investigate your claim.



Fourier ptychographic dark field x-ray microscopy

MADS CARLSEN,^{1,*}  TRYGVE M RÆDER,¹ CAN YILDIRIM,² RAQUEL RODRIGUEZ-LAMAS,² CARSTEN DETLEFS,²  AND HUGH SIMONS¹ 

¹Department of Physics, Technical University of Denmark, 2800 Kgs. Lyngby, Denmark

²ESRF, The European Synchrotron, 71 Avenue des Martyrs, CS40220, 38043 Grenoble Cedex 9, France

*madsac@dtu.dk

Abstract: Dark-field x-ray microscopy (DFXM) is an x-ray imaging technique for mapping three-dimensional (3D) lattice strain and rotation in bulk crystalline materials. At present, these maps of local structural distortions are derived from the raw intensity images using an incoherent analysis framework. In this work, we describe a coherent, Fourier ptychographic approach that requires little change in terms of instrumentation and acquisition strategy, and may be implemented on existing DFXM instruments. We demonstrate the method experimentally and are able to achieve quantitative phase reconstructions of thin film samples and maps of the aberrations in the objective lens. The method holds particular promise for the characterization of crystalline materials containing weak structural contrast.

© 2022 Optica Publishing Group under the terms of the [Optica Open Access Publishing Agreement](#)

1. Introduction

Since its recent introduction [1,2], Dark-field X-ray Microscopy (DFXM) has experienced growing use in the characterization of a wide range of materials and phenomena, from annealing in metals [3,4] to failure in battery materials [5] and domain wall dynamics in ferroelectric oxides [6]. DFXM differs from other diffractive x-ray microscopy techniques (e.g. Bragg coherent diffractive imaging — BCDI [7,8], Bragg ptychography — BP [9], Bragg projection ptychography — BPP [10], and x-ray ptychographic topography [11]) in that it does not measure far-field diffraction patterns, but rather records the intensity at an image plane. DFXM achieves this via the use of an objective lens placed in the scattered beam (see Fig. 1).

Compared to many other diffraction imaging methods, DFXM has larger a Field Of View (FOV, ≈ 0.1 mm) and lower spatial resolution, which makes it natural for studying larger samples. This in turn necessitates the use of x-rays with high photon energies (typically 15–30 keV) to be able to penetrate thick samples and, to some degree, to avoid dynamical scattering effects. As DFXM records intensity in an image plane, it is more natural to see DFXM as a modification of x-ray topography [12,13] in which the magnification is achieved by using an objective lens which enables higher spatial resolution (≈ 100 nm), and the small angular acceptance of the objective lens (≈ 1 mrad) facilitates quantitative mapping of components of the lattice strain and rotation. The procedure by which local lattice distortions are mapped requires sequentially collecting a series of images while rotating the sample about two axes orthogonal to the scattering vector and translating the objective lens through small steps transverse to the scattered optical axis. The strain and rotations of the crystal lattice are then extracted from the center-of-mass (COM) of the intensity distribution in each pixel in the image as a function of the lens position and/or sample rotation [1,14].

While the existing literature describing DFXM applies an incoherent model based on geometric optics, coherent diffraction techniques utilize a different scattering model that accounts for wave optical effects. As such, coherent models of imaging are more readily able to account for phase

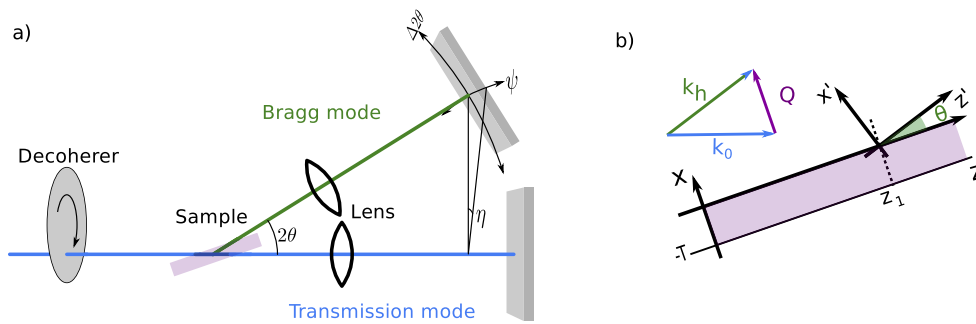


Fig. 1. a) Sketch of microscope geometry b) and coordinate systems used in scattering calculations.

contrast and image artifacts due to optical aberrations, and to correctly describe the scattering from strain-free crystal defects, such as inversion domains [15–17] and stacking faults [18,19].

In the case of BCDI, it is required that the diffracting volume is smaller than the coherence length of the incident radiation on the sample, limiting the technique to small samples (e.g. nanoparticles) and state-of-the-art coherent x-ray sources. This limitation does not apply in the case of BP and BPP, where a focusing/condensing optic is used *before* the sample to limit the coherently-illuminated volume. Such lens-based methods only require the incident radiation be transversely coherent over the aperture of the focusing/condensing optic and longitudinally coherent through the projected distance of the incident beam through the sample. This requirement can be readily achieved in the case of thin samples (e.g. epitaxial films [9] and nanowires [19]), where the reduced thickness of the sample limits this projection distance.

Lens-based coherent imaging can also be carried out with the lens placed *after* the sample. This is the case in Fourier ptychography (FP) [20,21], which facilitates an increase of the spatial resolution of an optical microscope beyond the diffraction limit set by the numerical aperture (NA) of the objective lens and corrects for aberrations in the objective lens. Although the original visible-light implementation involved changing the direction of illumination, FP can be equivalently accomplished by tilting and/or translating the objective lens [22,23]. DFXM is remarkably similar to FP in that it is a simple microscope whose operation involves acquiring images at different objective lens positions. Therefore, the acquisition strategy of a FP-based implementation of DFXM should be little different from its existing implementation.

DFXM is typically carried out using a compound refractive lens (CRL) as the objective lens. While Fresnel Zone Plates (FZPs) are effective at the lower end of DFXM's energy range [24], they lose efficiency at the higher energies required by strongly absorbing samples. At these high energies, elliptical mirrors have been used as condensing lenses [25], but they are not well suited as objective lenses due to their small angular acceptance. Multi-layer Laue lenses [26] (MLLs) are another promising option for high-resolution focusing lenses and have previously been used as an objective lens in full-field microscopy [27], at present however they are not widely available. Consequently, CRLs remain a common choice for focusing and imaging lenses at hard x-ray energies, and have been demonstrated extensively across a range of coherent and incoherent imaging applications, including BCDI [8].

In this paper, we describe how FP may be implemented within existing DFXM instruments, and demonstrate its use to reconstruct quantitative maps of structural distortions in an epitaxial film containing microscopic domain patterns and isolated screw dislocations. The experiments highlight several limitations and challenges, which are discussed in detail along with the merits of the approach.

2. Coherent x-ray scattering by strained crystals

The quantitative determination of lattice distortions via coherent diffractive x-ray microscopy techniques requires correlating the structural distortions to the phase of the sample's scattering function. Unlike the existing methods, the method we propose here does not resolve the scattering function in 3D but only the projection through the thickness of the film or, equivalently, the complex amplitude of the scattered wave front.

The fundamental quantity of interest is the spatially-dependent scattering function, $\chi'_h(\mathbf{r})$, first introduced by Takagi [28]:

$$\chi'_h(\mathbf{r}) = \exp(i\mathbf{Q} \cdot \mathbf{u}(\mathbf{r}))\chi_h \quad (1)$$

The constant χ_h is the Fourier coefficient of the electric susceptibility of a perfect crystal at wave vector \mathbf{Q} with Miller indexes hkl . $\mathbf{u}(\mathbf{r})$ is the displacement field at position $\mathbf{r} = [x, y, z]$. For simplicity, we work in a symmetric geometry where \mathbf{Q} is parallel to the x -axis and the scattering plane is normal to the y -axis. (see Fig. 1(b))

The phase of the scattering function is thus related to the strain and rotation of the crystal lattice. For thin films, where the intrinsic width of the rocking curve is large compared to the bandwidth and the vertical divergence of the incident beam, one can show that the phase gradients of the scattered beam are proportional to off-diagonal components of the strain-rotation tensor.

$$\begin{aligned} \frac{\partial \Phi}{\partial x'} &= -\frac{Q}{\sin(\theta)} \nabla \mathbf{u}_{1,3} \\ \frac{\partial \Phi}{\partial y'} &= Q \nabla \mathbf{u}_{1,2} \end{aligned} \quad (2)$$

where $\Phi(z, y)$ is the phase of the scattered field on the surface, Q is the magnitude of the scattering vector and $\nabla \mathbf{u}_{i,j}$ is the strain-rotation tensor, defined as:

$$\nabla \mathbf{u}_{i,j} = \frac{\partial u_i}{\partial r_j} \quad (3)$$

These phase gradients are related to the deflection of the scattered beam, away from the nominal direction, $\mathbf{k}_h = \mathbf{k}_0 + \mathbf{Q}$, where \mathbf{k}_0 is the average wave-vector of the incident radiation.

$$\begin{aligned} \Delta 2\theta &= 2\nabla \mathbf{u}_{1,3} \\ \psi &= 2 \sin \theta \nabla \mathbf{u}_{1,2} \\ \Leftrightarrow \eta &= \sec \theta \nabla \mathbf{u}_{1,2} \end{aligned} \quad (4)$$

This differs from the established equations in DFXM [2] for extended crystals, which operates under the opposite approximation: that the intrinsic rocking curve is narrow compared to the bandwidth and divergence of the incident radiation.

3. Implementation of Fourier ptychography in DFXM

In DFXM, the small numerical aperture (NA) of the objective lens acts as a low-pass filter on the image in the detection plane where the cut-off frequency is given by the physical aperture of the objective lens. The effect of translating the objective lens is to shift the position of this filter in frequency space by an amount proportional to the shift:

$$\mathbf{q}_s = \frac{\mathbf{s}}{\lambda d_1} \quad (5)$$

where \mathbf{s} is the 2D shift vector of the objective lens in real space, λ is the x-ray wavelength, d_1 is the effective sample-to-lens distance and \mathbf{q}_s is the displacement in frequency space in full period resolution.

Figure 2 shows how shifting the objective lens affects the contrast recorded by the detector. When the value of the shift falls within physical aperture of the lens (Fig. 2(b)), the images primarily contain information about the absolute value of the wave front. When it falls outside this aperture (Fig. 2(c)), the images contain information about the phase gradients (e.g. strains) and high-resolution features of the sample. At intermediate shifts (Fig. 2(d)), the images show a transition between these two regions, which appears as an image of the aperture.

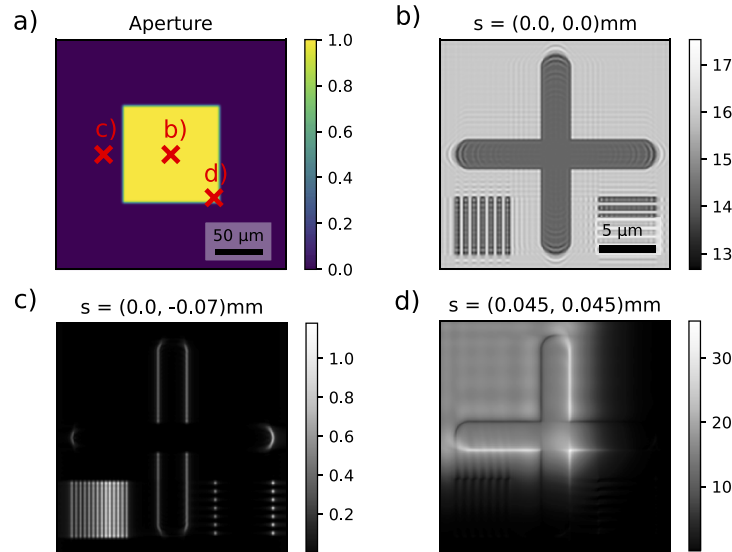


Fig. 2. Simulated microscope images displaying the nearfield behaviour. a) Aperture function $A(x,y)$ along with the shifts s used to calculate the images. b-d) simulated microscope images with different position of the objective lens as indicated in a). Simulation details are given in the [Supplement 1](#) section 2.

FP provides a means by which stacks of band pass-limited images obtained under appropriately frequency-shifted conditions can be computationally combined into a single, high-resolution, phase-resolved image of the sample. This is achieved by “stitching” in Fourier space. Simultaneously, a map of the aperture function of the objective lens may also be reconstructed, which includes the lens’ aberrations.

However, previous implementations of FP, including those both in the visible [20] and x-ray [22] regimes, cannot be simply applied to DFXM. Firstly, because it is not feasible to change the angle of illumination in DFXM due to the impracticality of rotating the x-ray source and absence of a high-NA condenser of the type used in synchrotron x-ray-based FP microscopy [22]. Instead, the objective lens must be scanned through the diffracted wave field. Secondly, DFXM typically makes use of CRLs instead of FZPs as used by [22] in their demonstration of FP. Unlike FZPs, CRLs behave as a thick lens, and need to be rotated simultaneously with their translations. Furthermore, large objective lens displacements, which are often necessary for samples with large strains, require the detector to be translated as well. This combined motion of objective and detector is equivalent to rotating the imaging setup around the sample.

The combination of FP and DFXM therefore presents a number of unique challenges that range from issues of partial coherence, optical aberrations to the alignment errors induced by insufficient accuracy of the objective translation, objective tilt, and detector position.

3.1. Aberrations in CRLs and partial coherence

At present, DFXM predominantly utilizes CRLs based on indented beryllium disks for the objective lens. Such lenses have high-frequency aberrations due to grain boundaries in the polycrystalline beryllium [29], which generate strong speckle contrast in the resulting images. In some cases, this speckle is stronger than the signal from the sample itself. To alleviate this issue, a decoherer, typically comprising a rotating disc of graphite, can be placed upstream of the sample [30]. This ensures that the sample is illuminated incoherently, which effectively averages out the speckle contrast stemming from the lens errors. Furthermore, the low coherence dampens the Fourier-ringing features in the images that arise from the hard edges of the aperture, as well as smoothing the image of the objective lens aperture that is seen in some images. Figures 3(a) and 3(b) show examples of simulated coherent and incoherent images with an objective lens containing high-frequency errors.

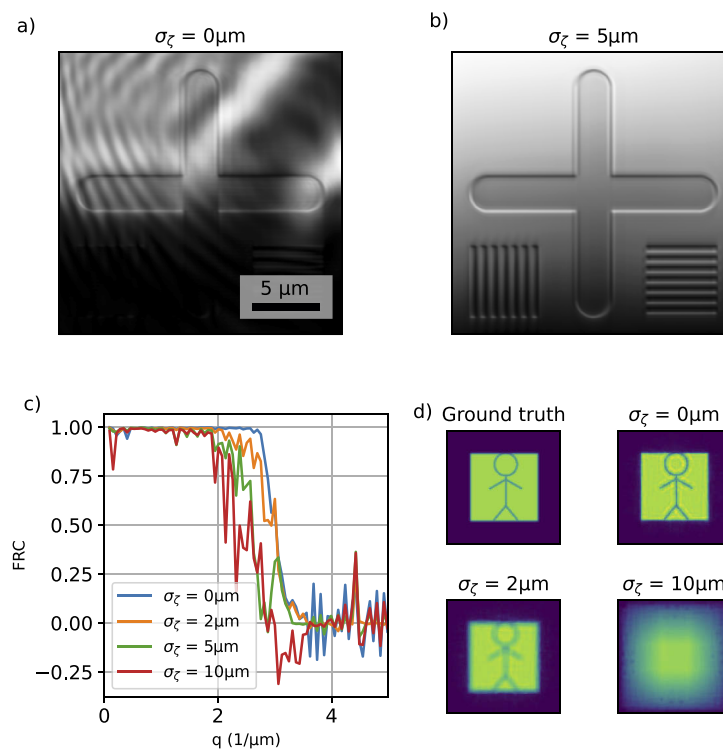


Fig. 3. a) Simulated coherent image with high-frequency errors in the lens function. b) Simulated incoherent image with high-frequency errors in the lens function. c) FRC of reconstruction with varying degrees of incoherent illumination. d) Reconstructed aperture function amplitude. Images of the reconstructed samples and apertures are shown in the [Supplement 1](#), Section 5

The use of a decoherer is problematic for FP because it assumes that the incident illumination is fully coherent. In practice, FP has been shown to be relatively stable towards partial coherence and it is sufficient to require the illumination be coherent over the extent of the coherent point spread function of the objective lens [31]. As such, we treat low partial coherence as a source of error and investigate the effect of partial coherence on FP by performing FP reconstructions on simulated data sets using an objective lens with high frequency aberrations and varying degrees of partial coherence.

The partially coherent images, I_{inc} , are simulated using Abbe's approach by evaluating the integral:

$$I_{\text{inc}}(x, y) = \int I_{\text{coh}}(x, y; s_x, s_y) p_{\sigma_z}(s_x, s_y) ds_x ds_y \quad (6)$$

where $I_{\text{coh}}(x, y; s_x, s_y)$ is the image that would be created by coherent plane wave illumination at an angle \mathbf{s}/d_1 and $p_{\sigma_z}(s_x, s_y)$ is a symmetric 2D normal distribution with variance σ_z^2 . The geometric parameters are approximately the same as those in the experiments detailed below.

To evaluate the quality of the reconstructions, we plot the Fourier ring correlation (FRC) [32] between the reconstructed sample functions and the ground truth used in the simulations (Fig. 3(c)). With full or high coherence, we can achieve an almost perfect FRC coefficient up until the full range covered by the scan. However, when a higher value of σ_z is used, the resolution of the reconstructions is lowered, but it is still able to reach the correct phases at low resolution. As expected, the reconstructed aperture functions (Fig. 3(d)) using a partially coherent source are approximately blurred versions of the ground truth aperture used to simulate the images.

In CDI and ptychography, partial coherence can be accounted for by including the effect of a partially coherent source in the forward model used in the reconstruction algorithm. In ptychography, this is done by a coherent mode decomposition of the incident beam [33].

In CDI, such a coherent mode decomposition into a few discrete modes is not appropriate due to the extended illumination. Rather, the illumination is decomposed into plane wave modes at different angles of incidence. This means that the partial coherence is included in the forward model by blurring the predicted data in reciprocal space [34]. For FP, such blurring in reciprocal space could also be applied, but as the data is collected in an image plane, this is not achieved by a simple convolution of the predicted image. A partially coherent forward model, as given by Eq. (6), could be used instead, but due to the large number of FFT operations necessary to calculate the integral, we found this model too slow to be used in the reconstruction procedure.

Ultimately, these simulations suggest that FP can be used for coherent image reconstruction of DFXM data, even under moderate degrees of partial coherence. This, in turn, provides some tolerance of the high-frequency lens errors associated with current CRLs.

3.1.1. Registration errors

Mechanical imprecision in the DFXM instrumentation leads to registration errors in the recorded images, due to small unknown displacements between the detector and the objective lens. Position errors of the lens are especially severe, since the resultant shift of the image on the detector is multiplied by the magnification factor minus one. The observed experimental errors are larger than the target resolution and, if not corrected for, these errors degrade the resolution of the reconstructions. (see Fig. 4)

We therefore propose and evaluate two different approaches to registration correction for FP-DFXM data sets, both of which rely on the scikit-image implementation of a super-sampling Fourier cross-correlation method [35]. The first method is a pre-processing step where all images are registered to an average of neighboring images in the data set, starting from that with the smallest shift. This approach is similar to that previously described in the literature [22]. The second approach updates the registration correction iteratively as a part of the FP reconstruction. The registration process involves iteratively: 1) reconstructing the sample based on the available data, 2) predicting the data based on the current iterate, 3) registering the images to the predicted data.

We evaluate these two methods by simulating a FP data set with random, known registration errors and perform reconstructions using the different registration approaches. Figure 4 shows that the first registration approach fails on the simulated data, and that the second, iterative, approach is able to achieve a reconstruction with an FRC correlation coefficient almost as high as

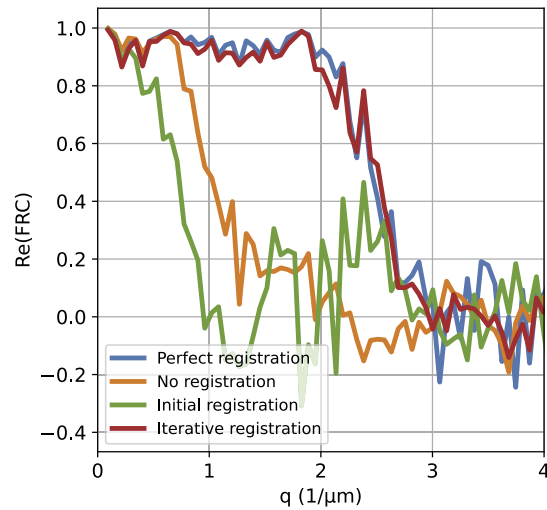


Fig. 4. FRC plots of simulated reconstructions with registration errors using different approaches to the registration correction. A detailed description of the registration corrections are given in the [Supplement 1](#), Section 4.

if the registration were carried out using the known error values. Details of implementation of the simulations and reconstructions are given in the [Supplement 1](#) section 3.

4. Experimental method

To demonstrate and evaluate the FP implementation on DFXM instrumentation, we carried out two experiments: First, in the transmission geometry using a commercial resolution calibration sample (JIMA RT-RC 04, Japan); and second, in the Bragg (i.e. dark-field) modality, using an epitaxial film of BiFeO_3 containing isolated dislocations and sub-micrometer domains. The DFXM measurement sampled the (002) pseudocubic reflection in a symmetric (i.e. specular) Bragg geometry. In both cases, data sets were recorded both with and without the decoherer.

The experiments were performed at the hard x-ray microscope at beamline ID06 [36] at the European Synchrotron (ESRF) at 17 keV with a relative bandwidth of $\approx 1.4 \cdot 10^{-4}$. The energy bandwidth and source size for the experiment were therefore typical of those expected for hard x-ray microscopy experiments. The microscope utilized an indirect scintillator detector with an effective pixel size of $0.75 \mu\text{m}$ and a CRL objective. The CRL comprised 70 individual biconcave beryllium lenses with radius of curvature $R = 0.05 \text{ mm}$. In transmission mode, the CRL was located $\approx 330 \text{ mm}$ from the sample and 4430 mm from the detector. The absorption in the lens material effectively creates a Gaussian-shaped aperture with width $\sigma = 0.13 \text{ mm}$ (FWHM = 0.31 mm). Notably, the severe aberrations of the lenses result in image resolution several times worse than the diffraction limit set by the width of this aperture. To limit the effect of these aberrations, we inserted a square absorbing aperture with full width 0.1 mm on the exit side of the CRL. The aperture does not visibly degrade the resolution of the resulting images and also ensures that the detector over-samples the objective lens by a factor of >2 (this oversampling is not a requirement of the method). The decoherer comprised a spinning disk of 1.5 mm -thick graphite, located 1650 mm upstream of the sample.

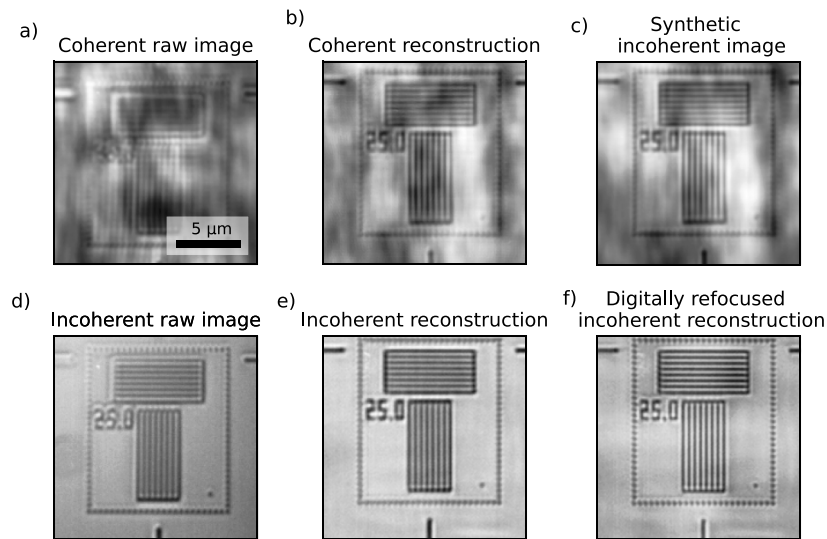


Fig. 5. Examples of raw images in transmission mode with a resolution target sample a) without and d) with the decoherer. And the absolute squares of the reconstructions made with images respectively without b) and with e) the decoherer in. c) a synthetic incoherent image made by summing over the registered images in the coherent data set. f) Amplitude of a digitally refocused version of the incoherent reconstruction. The line width is 250 nm.

5. Results and discussion

5.1. Transmission mode

In agreement with the earlier simulations, the raw images taken without the decoherer are contaminated by speckle-like noise due to the lens aberrations, this noise disappears when the decoherer is used (Fig. 5(a), 5(d)). We are able to achieve stable reconstructions with both data sets (Fig. 5(c), 5(e)), however the reconstruction based on data using the decoherer contains artefacts due to the lens aberrations. The reconstruction from the coherent data set is of similar **apparent** quality to that of the synthetic incoherent image generated by summing over the individual raw images in the same data set (see Fig. 5(b), 5(e)).

The recovered phase suffers from low-frequency artefacts, seen in Fig. 6(c) These errors arise because FP is not directly sensitive to the absolute phase, but only correlations in the phase function over the size of the coherent point spread function of the objective lens. The absolute phase must then be recovered by numerically integrating these correlations over the reconstructed region of interest.

The recovered phase shows clear signs that the sample is de-focused. We use the recovered complex amplitudes to digitally re-focus the reconstruction (details given in the [Supplement 1](#), Section 7). The digital re-focusing clearly improves the visibility of the features in the phase-image in Fig. 6(c), 6(d), while in the amplitude images Fig. 6(a), 6(b), the improvement is mainly evident by the increased visibility of the line of dots in the left hand side of the images.

The amplitude of the reconstructed phase delay over the narrow line-features is smaller (0.1 rad) than the theoretically expected value, which is calculated from the specification of the resolution target to be 0.62 radians. This discrepancy can be explained by a loss of contrast for small features close to the resolution limit. To evaluate the accuracy of the reconstructed phase-functions, we also reconstruct a different part of the same resolution target with larger features and find that the recovered phase-jump is smaller than the expected value by approximately 25%. A detailed description of this analysis can be found in the [Supplement 1](#), Section 8.

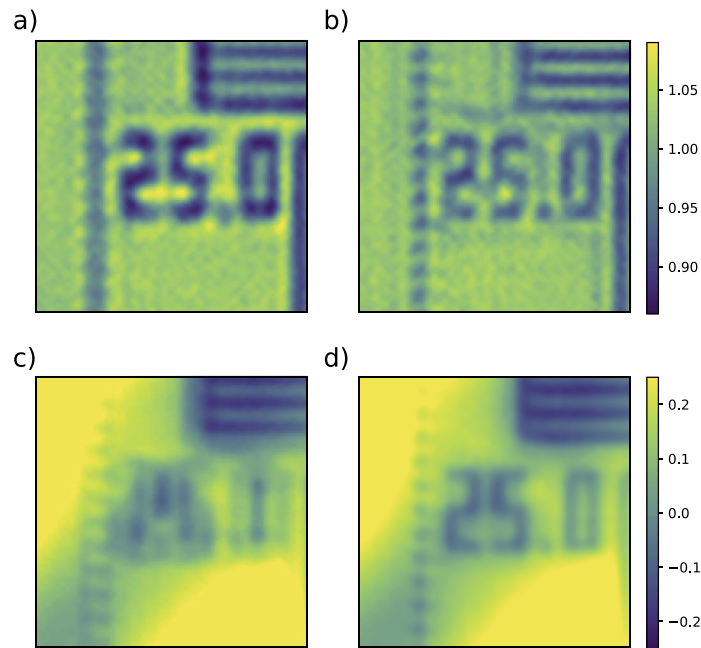


Fig. 6. Recovered a) amplitude and c) phase map of resolution test sample and refocused b) amplitude and d) phase. The phase images have been high-pass filtered to remove some reconstruction artifacts.

5.2. Bragg mode

The measurements in Bragg mode used the same measurements and reconstructions as in the transmission case, albeit with the optical axis rotated to the scattered beam ($2\theta \approx 22^\circ$). Examples of raw images and the absolute square of the reconstructions are shown in Fig. 7. Qualitatively, the reconstructions (Fig. 7(b), 7(e)) appear more detailed than individual raw images (Fig. 7(a), 7(c)), but that they do not contain significantly more detail than if the data sets were just summed (Fig. 7(c), 7(f)). We note that the high quality of the summed data set images shown here is dependent on the registration corrections acquired as a part of the iterative FP reconstruction. The speckle-like noise due to the lens aberrations is less noticeable in the Bragg-mode images shown in Fig. 7(e) and 7(f) than in the transmission-mode images of Fig. 7(a) and 7(b).

Reconstructions of the aperture function are shown in Fig. 8 respectively with and without the decoherer. As predicted by the simulations, FP with partially coherent illumination recovers a smooth aperture function which is approximately a blurred version of the “coherent” aperture. The recovered aperture in transmission mode (Fig. 8(c), 8(f)) shows some of the same features as the Bragg-mode apertures. The two aperture functions are not expected to be exactly identical as slightly different alignment of the lens between the two experiments, because of thick-lens effects, leads to a different effective aperture. The reconstructed aberrations from the transmission images appears to be stronger than the Bragg-mode reconstructions.

We estimate the resolution of the FP reconstructions by making two independent reconstructions, each using half of the data set but initialized with the registration correction obtained by a full reconstruction. Figure 9 shows the FRC between two such reconstructions of the incoherent data set. We achieve an effective half-period resolution of between $0.2 \mu\text{m}$ and $0.1 \mu\text{m}$ for the incoherent reconstruction, which is well above the diffraction limit for a single image. For comparison, we also show the FRC calculated between the two first images in the data set.

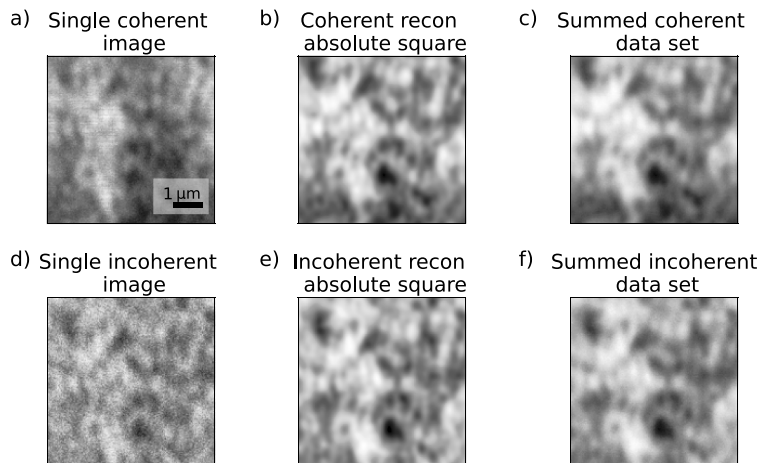


Fig. 7. Comparison of different images and reconstructions in the Bragg-mode. a,d) Examples of raw images at low shift. b,e) absolute square of FP reconstructions, c,f) sum over data sets. a-c) without and d-f) with the decoherer.

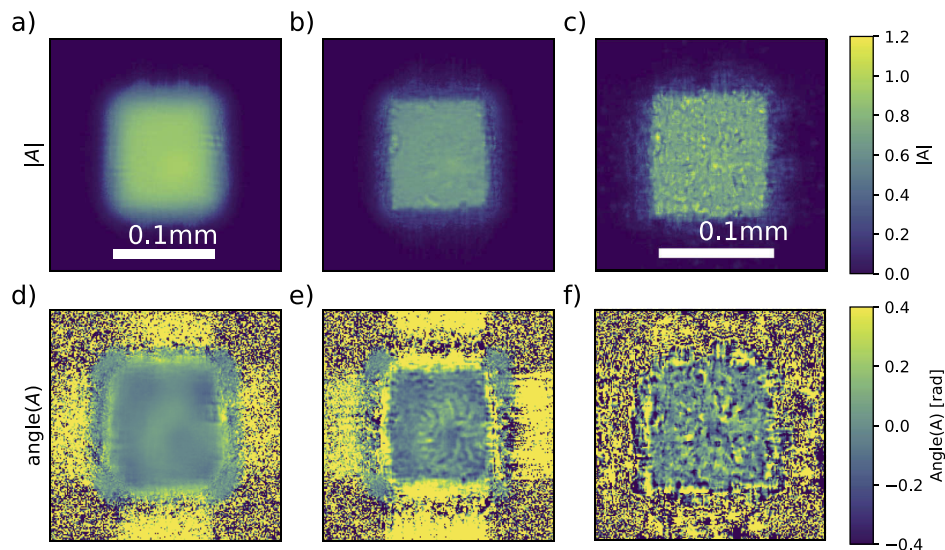


Fig. 8. Amplitude (a,b,c) and phase (d, e, f) maps of recovered aperture functions recovered with FP in Bragg mode respectively with (a,d) and without (b,e) a decoherer. And (c,f) the apertures recovered in transmission mode without the decoherer. The scale bar in a) applies also for (b, d, e) and the scale bar in c) applies for f as well.

The thin film sample used here poses a particular challenge for quantitative phase imaging methods. The dislocations in the sample generate phase vortices in the scattered field with a winding number given by the dot product of the Burger's vector with the hkl -vector. The unwrapped phase function that most quantitative phase microscopy methods try to recover therefore does not exist. However, as the FP algorithm considers only the real and imaginary parts of the amplitudes and not with an unwrapped phase-function, such phase vortices can be reconstructed. Such vortices cannot spontaneously appear in the FP reconstruction, however, and instead must emerge either from the boundary of the image or as a pair of opposite-handed

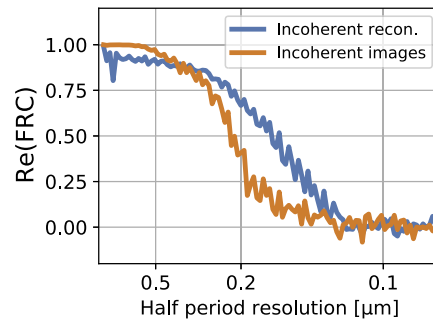


Fig. 9. Estimation of reconstruction resolution using two independent reconstructions each using half of the data set and the FRC correlation between the two images with the lowest reciprocal space shift.

vortexes, after which one vortex migrates to the image boundary over several iterations. In practice, this often causes the reconstruction to become stuck in local minimum. We therefore initialize a number of reconstructions with a different number of phase vortexes close to the dislocation and compare the reconstructions with the normal DFXM analysis, where the strain is inferred from the pixel-by-pixel Center-Of-Mass as a function of lens-position. Figure 10 shows the recovered phase gradients when the reconstructions have been initialized with zero and two phase vortexes, respectively. From comparison with the COM analysis, it is clear that only the reconstruction including the vortexes is consistent with the data.

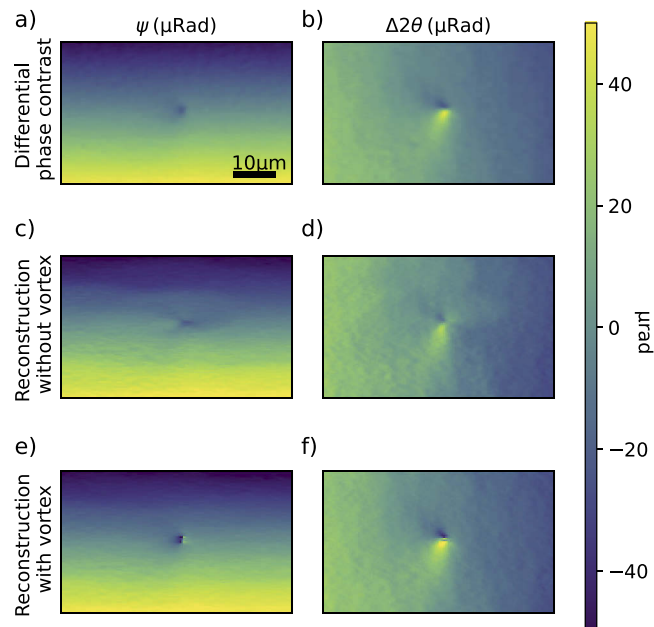


Fig. 10. Calculated deflection angles as defined in Eq. (4). a,b) are calculated from the COM of the image stack. c,d) are calculated using an FP reconstruction with no phase vortexes. e,f) are calculated using an FP reconstruction with a phase vortex of winding number 2. The reconstructions have been low-pass filtered to remove artefacts above the resolution limit of the reconstruction.

6. Conclusion and outlook

The reconstructed amplitude and phase maps from the BiFeO₃ film demonstrate that FP may be used for the coherent reconstruction of DFXM data sets. The resolution increase beyond that of diffraction limit set by the NA of the objective lens is marginal. However, we are able to recover the complex amplitude of the scattered wave front and the aperture function.

This ability to recover phase offers two key advantages over classical DFXM; the quantitative phase is critical when characterizing samples where contrast originates from strain-free defects. Furthermore, access to the quantitative phase allows us to correct for de-focus, which is readily seen in the current implementation of DFXM. At the same time, the phase- and amplitude maps of the objective aperture can be used to characterize x-ray lenses during their use as objective lenses for full field microscopy. This method appears more sensitive to the high-frequency (high order Zernike modes) aberrations (which generate strong speckle-like contrast in full field images) than grating interferometry [37] or speckle tracking [38].

Compared to other diffraction imaging techniques, DFXM offers the ability to characterize volumes inside bulk samples by illuminating the sample with a sheet beam, i.e. a beam extended in one direction but narrow (<1 μ m) in the other, such as is used in classical section topography [39]. Applying the FP analysis with such an illumination scheme would yield a “confocal microscopy” method similar to that suggested by AF. Pedersen and co-authors [40], albeit measuring in an image plane instead of a Fourier plane. Measuring in the image plane would mean that the acquisition strategy and instrumentation would be largely the same as in existing DFXM. However, such an “FP confocal microscopy” approach requires the illumination to be coherent over the aperture of the condensing lens, which at the existing DFXM instrument at ESRF would require placing a slit at the entry of the condensing lens. Doing so would increase the width of the condensed beam and decrease the flux on the sample, which may be a serious concern for this already flux-hungry technique.

Another potential concern is the viability of FP for analysing data sets from highly- and heterogeneously-deformed crystals. In such samples only a small volume of the crystal are in the diffracting Bragg condition at any one orientation. Because FP is only sensitive to short-range correlations, stable FP reconstructions require clean images with large areas of connected non-zero intensities to constrain the refinement of the aperture function. Less deformed (but still extended) crystals, however, give rise to dynamical diffraction patterns, where there is no simple connection between the scattered wave front and the lattice strains - a problem shared by any other x-ray diffraction technique.

In this work we only measured the projection of the scattering function through the direction of the scattered beam. However, a natural extension of this technique would be to attempt to resolve this depth dimension. This could potentially be achieved by “rocking” the sample through a small angle (as in BP and BCDI) and thus adding another dimension to the data set. In BPP, where the sample is not rocked, the depth dimension is resolved by back projecting different limited projections through the thickness of the sample. However, this approach is not compatible with the extended illumination used in this work, as we can only measure the projection through the full thickness.

While it is clear that the FP based DFXM approach demonstrated here has some drawbacks and limitations compared to both DFXM and other coherent techniques, we believe many of these issues can be remedied by adapting proven methods from similar techniques and, in particular, the development of better, less aberrated hard x-ray lenses. In this case, the technique should open significant opportunities for improving the amount of information achievable using DFXM.

Funding. European Research Council (804665).

Acknowledgments. The authors are grateful to the ESRF for providing beamtime on beamline ID06.

Disclosures. The authors declare no conflicts of interest

Data availability. Data underlying the results presented in this paper are not publicly available at this time but may be obtained from the authors upon reasonable request.

Supplemental document. See [Supplement 1](#) for supporting content.

References

1. H. Simons, A. King, W. Ludwig, C. Detlefs, W. Pantleon, S. Schmidt, F. Stöhr, I. Snigireva, A. Snigirev, and H. F. Poulsen, "Dark-field x-ray microscopy for multiscale structural characterization," *Nat. Commun.* **6**(1), 6098 (2015).
2. H. F. Poulsen, A. C. Jakobsen, H. Simons, S. R. Ahl, P. K. Cook, and C. Detlefs, "X-ray diffraction microscopy based on refractive optics," *J. Appl. Crystallogr.* **50**(5), 1441–1456 (2017).
3. S. R. Ahl, H. Simons, Y. B. Zhang, C. Detlefs, F. Stohr, A. C. Jakobsen, D. J. Jensen, and H. F. Poulsen, "Ultra-low-angle boundary networks within recrystallizing grains," *Scr. Mater.* **139**, 87–91 (2017).
4. N. Mavrikakis, C. Detlefs, P. K. Cook, M. Kutsal, A. P. C. Campos, M. Gauvin, P. R. Calvillo, W. Saikaly, R. Hubert, H. F. Poulsen, A. Vaugeois, H. Zapolsky, D. Mangelinck, M. Dumont, and C. Yildirim, "A multi-scale study of the interaction of Sn solutes with dislocations during static recovery in α -Fe," *Acta Mater.* **174**, 92–104 (2019).
5. C. Chen, T. Zhou, D. L. Danilov, L. Gao, S. Benning, N. Schoen, S. Tardif, H. Simons, F. Hausen, T. U. Schulli, R.-A. Eichel, and P. H. L. Notten, "Impact of dual-layer solid-electrolyte interphase inhomogeneities on early-stage defect formation in Si electrodes," *Nat. Commun.* **11**(1), 3283 (2020).
6. J. Ormstrup, E. Ostergaard, V. C. Detlefs, R. H. Mathiesen, C. Yildirim, M. Kutsal, P. K. Cook, Y. Watier, C. Cosculluela, and H. Simons, "Imaging microstructural dynamics and strain fields in electro-active materials in situ with dark field x-ray microscopy," *Rev. Sci. Instrum.* **91**(6), 065103 (2020).
7. M. A. Pfeifer, G. J. Williams, I. A. Vartanyants, R. Harder, and I. K. Robinson, "Three-dimensional mapping of a deformation field inside a nanocrystal," *Nature* **442**(7098), 63–66 (2006).
8. S. Maddali, J.-S. Park, H. Sharma, S. Shastri, P. Kenesei, J. Almer, R. Harder, M. J. Highland, Y. Nashed, and S. O. Hruszkewycz, "High-energy coherent x-ray diffraction microscopy of polycrystal grains: Steps toward a multiscale approach," *Phys. Rev. Applied* **14**(2), 024085 (2020).
9. S. O. Hruszkewycz, M. V. Holt, C. E. Murray, J. Bruley, J. Holt, A. Tripathi, O. G. Shpyrko, I. McNulty, M. J. Highland, and P. H. Fuoss, "Quantitative Nanoscale Imaging of Lattice Distortions in Epitaxial Semiconductor Heterostructures Using Nanofocused X-ray Bragg Projection Ptychography," *Nano Lett.* **12**(10), 5148–5154 (2012).
10. S. O. Hruszkewycz, M. Allain, M. V. Holt, C. E. Murray, J. R. Holt, P. H. Fuoss, and V. Chamard, "High-resolution three-dimensional structural microscopy by single-angle Bragg ptychography," *Nat. Mater.* **16**(2), 244–251 (2017).
11. M. Vezzhak, S. Van Petegem, A. Rodriguez-Fernandez, P. Godard, K. Wakonig, D. Karpov, V. L. R. Jacques, A. Menzel, L. Thilly, and A. Diaz, "X-ray ptychographic topography: A robust nondestructive tool for strain imaging," *Phys. Rev. B* **103**(14), 144107 (2021).
12. W. Berg, "Roentgenographic methods for investigating lattice imperfections in crystals," *Naturwissenschaften* **19**(19), 391–396 (1931).
13. B. Tanner, "X-Ray Diffraction Topography: International Series in the Science of the Solid State," International series in the science of the solid state (Elsevier Science, 2013).
14. H. F. Poulsen, L. E. Dresselhaus-Marais, M. A. Carlsen, C. Detlefs, and G. Winther, "Geometrical-optics formalism to model contrast in dark-field X-ray microscopy," *J. Appl. Crystallogr.* **54**(6), 1555–1571 (2021).
15. H. Klapper, "X-Ray Topography of Twinned Crystals," *Prog. Cryst. Growth Charact. Mater.* **14**, 367–401 (1987).
16. P. Rejmankova-Pernot, P. Cloetens, J. Baruchel, J. Guigay, and P. Moretti, "Phase retrieval by combined Bragg and fresnel X-ray diffraction imaging," *Phys. Rev. Lett.* **81**(16), 3435–3438 (1998).
17. S. Labat, M.-I. Richard, M. Dupraz, M. Gailhanou, G. Beutier, M. Verdier, F. Mastropietro, T. W. Cornelius, T. U. Schuelli, J. Eymery, and O. Thomas, "Inversion Domain Boundaries in GaN Wires Revealed by Coherent Bragg Imaging," *ACS Nano* **9**(9), 9210–9216 (2015).
18. G. Kowalski, A. Lang, A. Makepeace, and M. Moore, "Studies of Stacking-Fault Contrast by Synchrotron X-ray Section Topography," *J. Appl. Crystallogr.* **22**(5), 410–430 (1989).
19. M. O. Hill, I. Calvo-Almazan, M. Allain, M. V. Holt, A. Ulvestad, J. Treu, G. Koblmüller, C. Huang, X. Huang, H. Yan, E. Nazaretski, Y. S. Chu, G. B. Stephenson, V. Chamard, L. J. Lauhon, and S. O. Hruszkewycz, "Measuring Three-Dimensional Strain and Structural Defects in a Single InGaAs Nanowire Using Coherent X-ray Multiangle Bragg Projection Ptychography," *Nano Lett.* **18**(2), 811–819 (2018).
20. G. Zheng, R. Horstmeyer, and C. Yang, "Wide-field, high-resolution Fourier ptychographic microscopy," *Nat. Photonics* **7**(9), 739–745 (2013).
21. P. C. Konda, L. Loetgering, K. C. Zhou, S. Xu, A. R. Harvey, and R. Horstmeyer, "Fourier ptychography: current applications and future promises," *Opt. Express* **28**(7), 9603–9630 (2020).
22. K. Wakonig, A. Diaz, A. Bonnini, M. Stampanoni, A. Bergamaschi, J. Ihli, M. Guizar-Sicairos, and A. Menzel, "X-ray Fourier ptychography," *Sci. Adv.* **5**(2), 1 (2019).
23. C. Detlefs, M. A. Beltran, J.-P. Guigay, and H. Simons, "Translative lens-based full-field coherent X-ray imaging," *J. Synchrotron Radiat.* **27**(1), 119–126 (2020).
24. K. Li, M. J. Wojcik, R. Divan, L. E. Ocola, B. Shi, D. Rosenmann, and C. Jacobsen, "Fabrication of hard x-ray zone plates with high aspect ratio using metal-assisted chemical etching," *Journal of Vacuum Science & Technology B* **35**(6), 06G901 (2017).

25. J. C. da Silva, A. Pacureanu, Y. Yang, S. Bohic, C. Morawe, R. Barrett, and P. Cloetens, "Efficient concentration of high-energy x-rays for diffraction-limited imaging resolution," *Optica* **4**(5), 492–495 (2017).
26. J. Maser, G. B. Stephenson, S. Vogt, W. Yun, A. Macrander, H. C. Kang, C. Liu, and R. Conley, "Multilayer Laue lenses as high-resolution x-ray optics," in *Design and Microfabrication of Novel X-Ray Optics II*, vol. 5539 A. A. Snigirev and D. C. Mancini, eds., International Society for Optics and Photonics (SPIE, 2004), pp. 185–194.
27. K. T. Murray, A. F. Pedersen, I. Mohacsi, C. Detlefs, A. J. Morgan, M. Prasciolu, C. Yildirim, H. Simons, A. C. Jakobsen, H. N. Chapman, H. F. Poulsen, and S. Bajt, "Multilayer laue lenses at high x-ray energies: performance and applications," *Opt. Express* **27**(5), 7120–7138 (2019).
28. S. Takagi, "Dynamical theory of diffraction applicable to crystals with any kind of small distortion," *Acta Crystallogr.* **15**(12), 1311–1312 (1962).
29. I. Lyatun, P. Ershov, I. Snigireva, and A. Snigirev, "Impact of beryllium microstructure on the imaging and optical properties of X-ray refractive lenses," *J. Synchrotron Radiat.* **27**(1), 44–50 (2020).
30. K. V. Falch, C. Detlefs, M. S. Christensen, D. Paganin, and R. Mathiesen, "Experimental investigation of gaussian random phase screen model for x-ray diffusers," *Opt. Express* **27**(15), 20311–20322 (2019).
31. R. Horstmeyer and C. Yang, "A phase space model of fourier ptychographic microscopy," *Opt. Express* **22**(1), 338–358 (2014).
32. W. Saxton and W. Baumeister, "The Correlation Averaging of a Regularly Arranged Bacterial-Cell Envelope Protein," *Journal of Microscopy-Oxford* **127**(2), 127–138 (1982).
33. P. Thibault and A. Menzel, "Reconstructing state mixtures from diffraction measurements," *Nature* **494**(7435), 68–71 (2013).
34. J. Clark, X. Huang, R. Harder, and I. Robinson, "High-resolution three-dimensional partially coherent diffraction imaging," *Nat. Commun.* **3**(1), 993 (2012).
35. M. Guizar-Sicairos, S. T. Thurman, and J. R. Fienup, "Efficient subpixel image registration algorithms," *Opt. Lett.* **33**(2), 156–158 (2008).
36. M. Kutsal, P. Bernard, G. Berruyer, P. K. Cook, R. Hino, A. C. Jakobsen, W. Ludwig, J. Ormstrup, T. Roth, H. Simons, K. Smets, J. X. Sierra, J. Wade, P. Wattercamp, C. Yildirim, H. F. Poulsen, and C. Detlefs, "The ESRF dark-field x-ray microscope at ID06," *IOP Conf. Ser.: Mater. Sci. Eng.* **580**(1), 012007 (2019).
37. T. Weitkamp, B. Nöhammer, A. Diaz, C. David, and E. Ziegler, "X-ray wavefront analysis and optics characterization with a grating interferometer," *Appl. Phys. Lett.* **86**(5), 054101 (2005).
38. S. Berujon, R. Cojocar, P. Piau, R. Celestre, T. Roth, R. Barrett, and E. Ziegler, "X-ray optics and beam characterization using random modulation: experiments," *J. Synchrotron Radiat.* **27**(2), 293–304 (2020).
39. A. Lang, "A Method for the Examination of Crystal Sections using Penetrating Characteristic X-Radiation," *Acta Metall.* **5**(7), 358–364 (1957).
40. A. F. Pedersen, V. Chamard, and H. F. Poulsen, "Confocal Bragg ptychography for bulk specimens: a numerical demonstration," *Opt. Express* **28**(11), 15770–15782 (2020).